

# B9 Report: An Investigation of the Brighter-Fatter Effect with CCD E2V-250



**Candidate Name:** Mingyu Liu 1024507

**Project Number:** B9\_05 Experimental

**Supervisor:** Dr. Daniel Weatherill

**Advisor:** Prof. Ian Shipsey

A report submitted for the degree of  
*BA Physics*  
Trinity 2020

# Abstract

Charge-coupled devices (CCDs) are regular lattices of charge receivers widely used in astronomical imaging. CCDs are generally considered to convert incoming photons into a digital number in each pixel in a linear fashion independent of the condition of surrounding pixels. However, it has been known for some time that the photon transfer curves (PTCs) of flat-field images taken by thick CCDs display abnormal deviations from the expected Poisson photon noise and that the point spread functions (PSFs) of star illuminations tend to broaden with increasing luminosity. This effect is commonly known as the “Brighter-Fatter Effect” (BFE). This investigation is carried out at the Oxford Physics Microstructure Detector (OPMD) laboratory using an electro-optical test system designed for optimising the operation of CCDs for use in the Large Synoptic Survey Telescope (LSST). First, several stability tests and calibration are carried out to verify the high measurement precision of the test system. Next, the investigation studies the brighter-fatter effect of flat-field images by observing the behaviour of the PTC and correlation maps between neighbouring pixels. A quadratic departure of PTC from Poisson statistics and linearly increasing pixel correlations with flux are observed. The correlation coefficients are found to decay rapidly with spatial separation. Finally, an electrostatic model that simulates the interaction between the Coulomb field induced by charges stored in CCD pixels and the drift field is presented to explain the observed statistical properties.

## 1 Introduction

A charge-coupled device (CCD) is a regular lattice of charge receiver which converts incoming light into digital number in a linear fashion. They are widely used in modern astronomical telescopes to carry out low-noise and high-dynamic-range imaging. In the camera design for astronomical telescopes, it is generally assumed that the response of a CCD pixel to a source of light scales linearly with the incoming flux, independent of the content of the surrounding pixels. Obviously, the scaling breaks down at some points as saturation is reached either in the sensor (charge buckets overflow) or in the electronic chain (signals saturate). However, this scaling breaks well before saturation is reached, due to an effect commonly known as the “Brighter-Fatter Effect” (BFE) [6]. This phenomenon causes distortion to images taken by many astronomical telescopes, most notably the Large Synoptic Survey Telescope (LSST) that requires measuring the shape of celestial objects to high precision. This introduction first explains the photon transfer curve (PTC), a powerful tool that characterises many key performance parameters of a camera system and is central to the following analyses. Then, the section reviews a history of the study of the BFE. Lastly, a brief overview of the LSST project and the instrumentation is given.

### 1.1 Photon Transfer Curve (PTC)

Photon transfer curve (PTC) is the response from a CCD sensor that is uniformly illuminated at different levels of flux. It is typically plotted as the signal variance  $\sigma^2$  against the mean  $\mu$  for a group of pixels contained on the CCD array. Figure 1 below shows a PTC taken from Janesick, James R. [7] on log-log scale

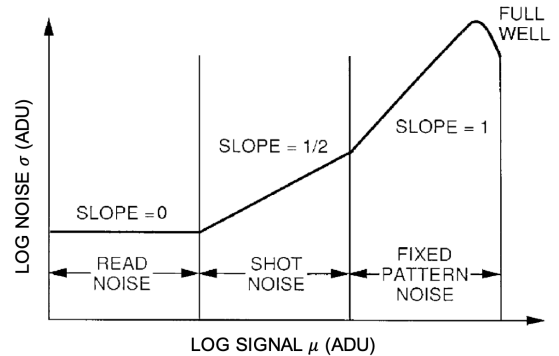


**Figure 1:** Typical photon transfer curve (PTC) on log-log scale. Three noise regimes can be identified: read noise dominant ( $k = 0$ ), shot noise dominant ( $k = 1/2$ ) and fixed-pattern noise dominant ( $k = 1$ ) before the full well is reached

Three noise regimes are identified in the plot:

**Regime 1:** Readout noise  $\sigma_R$  dominates when the signal level is low. It includes any noise source that is independent of the signal, which mainly comes from the downstream electronics (e.g. output amplifier) during the conversion of electrons into the digital unit.

**Regime 2:** Shot noise  $\sigma_S$  dominates as the illumination on the CCD increases. Shot noise is induced because the arrival of photons onto each pixel is governed by a random Poisson process, due to the quantised nature of light. This suggests that the variance of signal in any given pixel is expected to be equal to the mean  $\sigma_S^2 = \mu$  (hence the shot noise  $\sigma_S = \sqrt{\mu}$ ).<sup>1</sup>

**Regime 3:** The last regime is associated with the fixed-pattern noise (FPN) that comes from responsivity variations among pixels, typically due to pixel size and material differences. The fixed-pattern noise scales with the signal mean value and consequently produces a slope of unity on the log-log diagram. The onset of the full well is observed at the end of the regime and is characterised by a break in the slope of unity.

In this investigation, a pair of uniformly illuminated images (flat-fields) is collected at each luminosity during experiments. The flat-field PTC is generated using

<sup>1</sup>Note that a second independent source of shot noise comes from electrons (as opposed to the photons), due to the quantum yield of the sensor higher than one electron per photon. This happens mainly for high energy photons (e.g. deep UV). This project, however, is operated in the optical (visible) spectrum where the quantum yield of the sensor is one and the shot noise of electrons can be neglected.

the difference between the two frames, such that the fixed-pattern noise is eliminated. The readout noise of the CCD is very low  $\approx 4$  electrons compared to the full well capacity  $\approx 70,000$  electrons. Therefore, the photon transfer curve (PTC) plotted using the differenced frame is expected to be shot noise dominant, where the relationship between variance and mean is linear with a constant of proportionality equal to one.

The gain  $G$  of a CCD is the conversion between an arbitrary digital unit (ADU) specific to the CCD into the physical unit of electrons (el). It is expressed in the unit of  $el/ADU$  and can be found from the slope of the PTC (assuming Poisson statistics) via the simple equation.

$$G = \frac{S(ADU)}{\sigma_S^2(ADU)} \quad (1)$$

The gain  $G$  is key to standardising the PTCs across different channels, each configured with a different gain, and making meaningful comparisons between them.

## 1.2 Brighter-Fatter Effect

The present evolution in telescope camera design, moving from thinned CCDs to thick CCDs, corresponds to increased quantum efficiency, reduction of fringing and controlled spatial resolution. This evolution is thanks largely to the improvement of silicon wafer resistivity, which allows for full depletion of mobile charge carriers over several hundred microns [6].

It was first observed in 2006 by Downing, Mark, et al. that charge collection processes in thick CCD pixels were sensitive to their environment [5]. After eliminating all possible causes of non-linearity, including the CCD output amplifier, analogue-to-digital converter (ADC) and other downstream electronic chains, analysis of the flat-field illuminated images showed a positive statistical correlation between neighbouring pixel values. This flattens out the PTC as the flux increases, destroying the linearity as anticipated by Poisson statistics.

The physical mechanism suggested in the early work was that electrons might be thermally migrating between pixels during charge collection [9]. It was shown later that the alterations to the drift electric field caused by charges already collected in the potential wells of the CCD offered a more realistic explanation [1] [4]. The perturbation tends to drive drifting charges away from pixels with higher counts than their surroundings (hence the name “Brighter-Fatter Effect”). The same mechanism causes broadening of stars on astronomical images observed in 2014 with MegaCam hosted on the Canada-France-Hawaii 3.6-m Telescope (CFHTLS) and camera used in Sloan Digital Sky Survey (SDSS) [8].

## 1.3 LSST and CCD E2V-250

This project is performed in the Oxford Physics Microstructure Detector (OPMD) Laboratory with the

aim of improving the performance of the camera of the LSST. The LSST is an astronomical observatory currently under construction in Chile and is planned to be operational in 2022 to carry out wide, fast and deep surveys of the sky.<sup>2</sup> Of the four major scientific goals of the LSST project [10], the investigation of dark energy via weak gravitational lensing requires measurement of the ellipticity of distant sources to the precision of 0.1%.<sup>3</sup> However, the magnitude of the error caused by the BFE has been shown to be up to several per cents in some CCDs. [12] A correction method for the BFE is crucial to achieving the scientific goals.

The LSST camera consists of 189 CCD sensors at the focal plane, half of which are the CCD E2V-250. Each CCD E2V-250 is built up of  $4096 \times 4096$  ( $4K \times 4K$ ) imaging elements,  $100\mu m$  in thickness and equipped with sixteen amplifier channels. Each pixel is  $10\mu m$  wide and incorporated with four collection gate electrodes. One such CCD in OPMD will be used in this investigation.

## 2 Experimental Setup

A test stand has been designed in the OPMD laboratory to test the LSST CCD E2V-250. The primary light source is a Quartz Tungsten Halogen (QTH) lamp that illuminates a monochromator with an order sorting filter. The output from the monochromator is coupled via a liquid light guide to the input port of a beam splitter. For the purpose of this investigation, however, a GaP LED with a typical peak wavelength at  $556nm$  and bandwidth (FWHM) =  $40nm$  is used as the primary light source because the full well capacity of the CCD can be reached under much shorter experiment time, as the LED source is much brighter. Illumination at multiple wavelengths is not required in the flat-field experiment.

One port of the beam splitter is connected to a visible spectrometer to obtain the spectral content of the light source. Another port is connected to a 6” integrating sphere that monitors the intensity of the light source with a calibrated photodiode and produces a spatially uniform outgoing beam. The test stand is mounted on an active pneumatically controlled optical table of  $900mm \times 1200mm$  to eliminate vibration. A photograph of the whole system is shown in Figure 2.

A baffle tube of length 1m connects the output port of the integrating sphere to the testing cryostat. The interior of the tube is coated with black flocked paper and mounted with a rectangular knife-edge baffle. The geometry of the tube and baffle combination is chosen

<sup>2</sup>Wide: covering a large area of the visible sky; Fast: covering the area every few nights; Deep: able to detect very faint sources.

<sup>3</sup>Put it in simple terms, weak gravitational lensing refers to measuring the change in the shape of distant sources, due to deflection of photons caused by the distribution of matters between the source and the observers

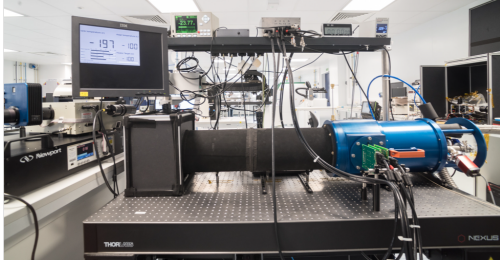


**Figure 2:** Optical test system at OPMD [11]

such that all stray rays arising from up to one reflection are removed.

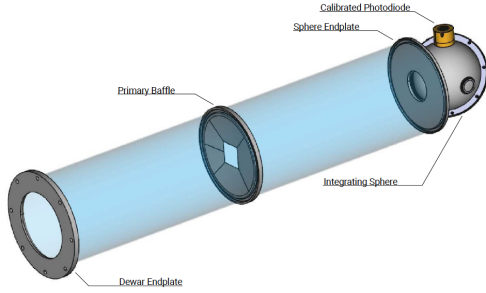


**Figure 3:** Baffle tube configuration [11]

The CCD under test itself is housed in an aluminium cryostat, which is evacuated to high vacuum using a turbopump and cooled below the operating temperature of  $-95^{\circ}\text{C}$  using liquid nitrogen (LN2). The operating temperature is maintained with a 25W heater. The readout and clocking of the CCD are controlled by the foxtrot software [13] developed by OPMD. A schematic of the cryostat configuration is shown in Figure 4.

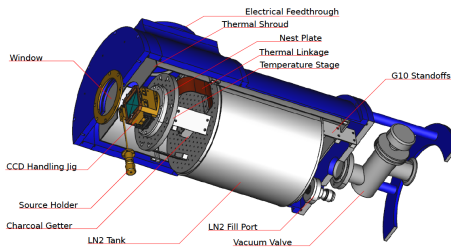


**Figure 4:** Partial cutaway view of the cryostat configuration [11]

The main contributions of this investigation are the following: a) verify the high power and wavelength stability of the throughput of the test system at OPMD b) calibrate the power and the spectral measurement c) illustrate the PTC non-linearity and linearly increasing correlations between neighbouring pixels d) demonstrate the dependence of the brighter-fatter effect on the backside substrate (BSS) voltage and collection gate width.

### 3 Tests and Calibrations

In this section, several tests and calibration performed on the test system are presented. The section consists of four parts. Section 3.1 demonstrates the high power stability of the LED source. High stability is required for the fixed-pattern noise between a pair of images taken at the same exposure to be removed so that any remaining noise is composed of shot noise. Section 3.2 outlines the methods of smoothing and calibrating raw spectrometer measurements. Section 3.3 proceeds on illustrating the wavelength stability of the LED source with the calibrated spectrometer. Section 3.4 estimates the level of bias introduced to the measured power as a consequence of using photodiode responsivity at a single wavelength instead of the weighted value over the spectrum.

#### 3.1 Intensity Stability Test

500 power readings are taken with the photodiode over a duration of 4.17 hours with 30s intervals between consecutive measurements, in both the integrating sphere and the environment. Histograms of the measurements are plotted in the upper panel of Figure 5. The power of the LED measured inside the integrating sphere has an average  $(7.329 \pm 0.009) \times 10^{-7} \text{ W/cm}^2$ , or equivalently a fractional uncertainty of 0.12%. The level of uncertainty is of the same order of magnitude as the photodiode measurement precision 0.15% (as in the manual), indicating that the time-variation in the LED power output is low and at a level undetectable by the resolution of our current instrumentation. Time series of the two measurements are plotted at the bottom of Figure 5. Their Pearson correlation coefficient is very low at  $r = -0.046$ , suggesting no evidence of stray light leakage into the optical system.

#### 3.2 Spectrometer Calibration

Raw spectra measured by the spectrometer need to be cleaned and calibrated before actual spectral contents can be obtained. The first step is to remove the bias offset introduced by the analogue-to-digital converter in the downstream circuitry. Bias offset corresponds to the spectrometer's output value in the total absence of signal photons and should be subtracted from the reading. It can be found for each reading by applying a highpass filter to eliminate the actual signal, and the remaining low-frequency signal represents the bias. The second step is to remove outliers caused by bad pixels on the digital sensor. A point is removed if the measured intensity at the point deviates from the median-filtered intensity by more than 10% of the peak intensity. The 10% threshold is carefully chosen to ensure that the points near the peak (which have steep slopes) are not falsely treated as outliers. The third step is to interpolate the values at the removed points using a second-order spline interpolation algorithm in Scipy (Scipy.interpolate.interp1d). The final

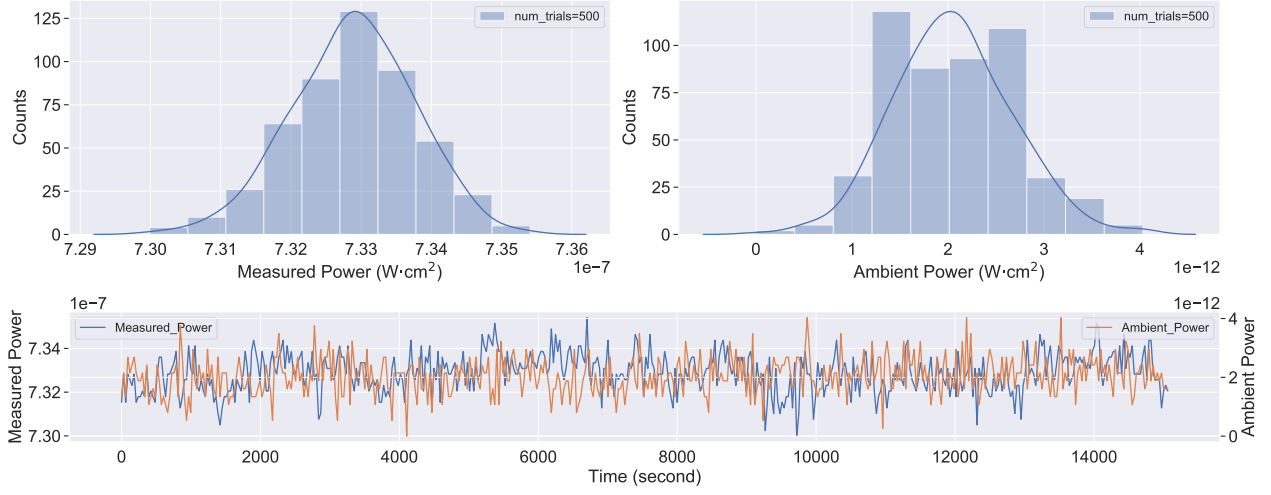


**Figure 5:** Measured power of the LED source and the environment in 500 repeated trials over a duration of 4.17 hours. Top Left: Histogram of LED power output measured inside the integrating sphere; Top Right: Histogram of ambient light power measured in the environment; Bottom: Time-series of the LED and ambient power

step is to smooth the spectrum. This is done using the savgol filter [2], a non-parametric digital filter for data smoothing. Twelve raw and processed spectra created using the QTH lamp and monochromator combination are plotted in Figure 6.

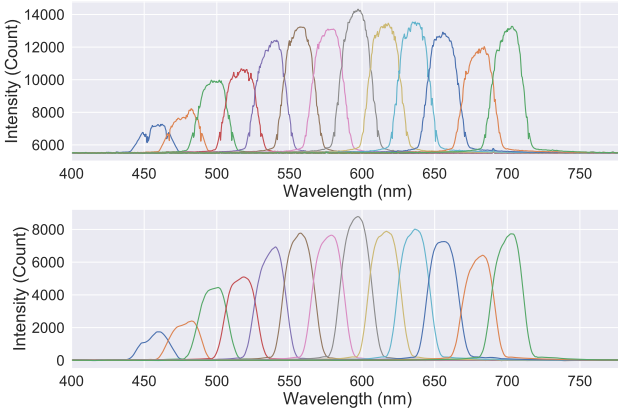


**Figure 6:** The spectra at 12 wavelengths of the Quartz Tungsten Halogen (QTH) lamp. Top: Raw spectrum; Bottom: Smoothed spectrum

Next, broadening of spectrum widths caused by the diffraction grating inside the spectrometer is corrected. The operation of the spectrometer relies on using a concave mirror to produce a collimated beam of the input light, dispersing it with a diffraction grating and measuring the intensities at different angles that corresponds to the first order maximum of various wavelengths. As the grating has a finite resolving power, even a highly monochromatic light would be dispersed into a finite band centred at the first-order maximum. The resultant measured spectrum is a convolution of the real spectrum with the interference pattern of the grating:

$$I(\theta) = \int I(\lambda) \times \frac{\sin(N\pi d \sin \theta / \lambda)}{N \sin(\pi d \sin \theta / \lambda)} d\lambda \quad (2)$$

where  $d$  denotes the separation between two reflecting elements and  $N$  denotes the total number of elements being illuminated. As the spectrometer measures the position of first-order maximum, the angle  $\theta$  is related to the labelled wavelength  $\bar{\lambda}$  via  $\sin(\theta) = \bar{\lambda}/d$ . Therefore, the integration above can be rewritten as

$$I(\bar{\lambda}) = \int I(\lambda) \times \frac{\sin(N\pi\bar{\lambda}/\lambda)}{N \sin(\pi\bar{\lambda}/\lambda)} d\lambda \quad (3)$$

To recover the actual spectrum  $I(\lambda)$  from  $I(\bar{\lambda})$ , the parameter  $N$  needs to be determined first. A diffused laser with a known spectrum is connected to the spectrometer to measure  $N$ . Fifty measurements of the laser's spectrum are taken, smoothed, normalised and averaged. The optimal value of  $N = 175$  is found by minimising the difference between the convolved and the measured spectrum using a grid search. The original, measured and fitted spectra are normalised and plotted in Figure 7.

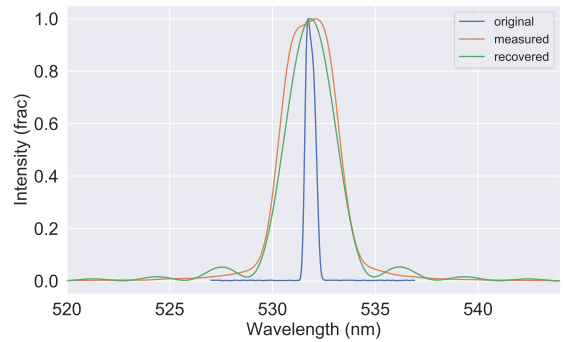


**Figure 7:** The real (blue), measured (orange) and fitted (green) spectra of the laser source. The optimal  $N = 175$  is found by minimising the difference between the convolved and the measured spectra, where  $N$  is the number of reflecting elements being illuminated.

In order to restore the real spectrum from the spectrometer reading, the inverse integral transform Equation 3 is performed. This is done numerically using matrix inversion. The inverse transform of the LED spectrum is plotted in Figure 8. The FWHM of the recovered spectrum is 36.3nm, a narrowing of 4.5% compared to the raw 38.0nm.

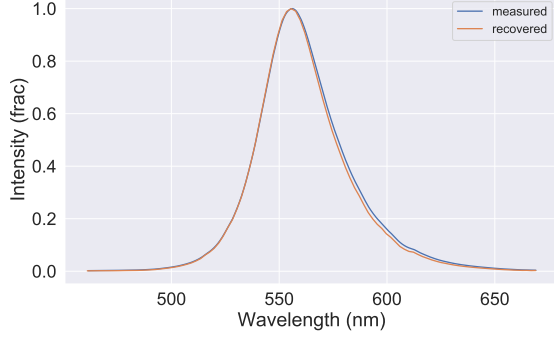


**Figure 8:** The measured (blue) and the recovered (orange) spectra of the LED source using the deconvolution method with the fitted  $N$

### 3.3 Wavelength Stability Test

Stability of the LED wavelength is tested by taking 500 spectrometer readings with 30-second intervals between consecutive measurements. The top panel of Figure 9 plots the histogram of the peak wavelengths, which follows a bell-shaped curve as expected. The bottom panel plots the peak intensity histogram. However, a wide non-Gaussian distribution is found, the reason for which has not been identified. Nevertheless, the purpose of the spectrometer is to measure the peak wavelengths and the shapes of spectra. Intensity is what the photodiode is for.

The peak intensities against total intensities (integrating the area below the power spectrum) are plotted in Figure 10. The relationship is linear with the r-squared value equal to 0.994, verifying the stability of the shape of the LED spectrum. The hue of each data point represents the peak wavelength. No correlation between the peak intensity and the peak wavelength is observed.

### 3.4 Power Measurement Bias

The photodiode takes raw measurement in current, which is converted to power by dividing a responsivity expressed in  $A/W \cdot cm^{-2}$ . The responsivity is initialised manually, corresponding to the value at the peak wavelength, before any measurement is taken. However, bias is inevitably induced in this conversion, as any real spectrum has a finite width that corresponds to a range of responsivity values. This section estimates the bias in the measured LED power using its power spectrum obtained above. Figure 11 plots

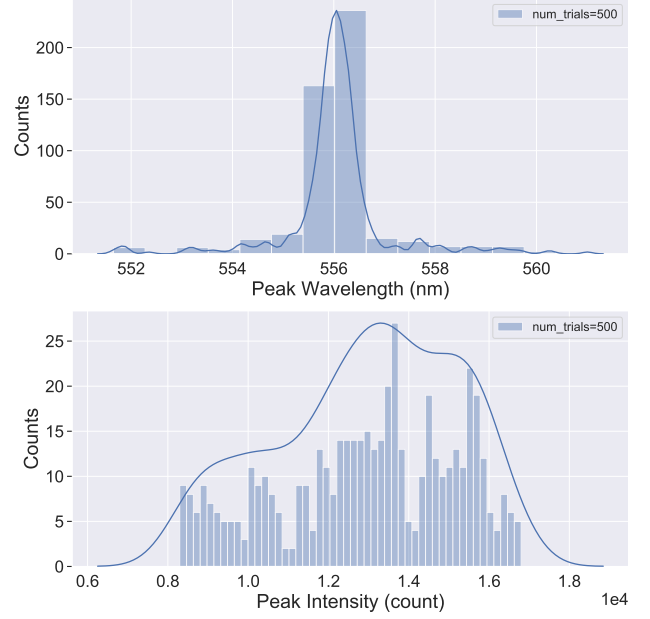


**Figure 9:** Measured peak wavelengths and intensities of the LED source for 500 repeated trials. Top: Histogram the peak wavelengths. Bottom: Histogram of peak intensities

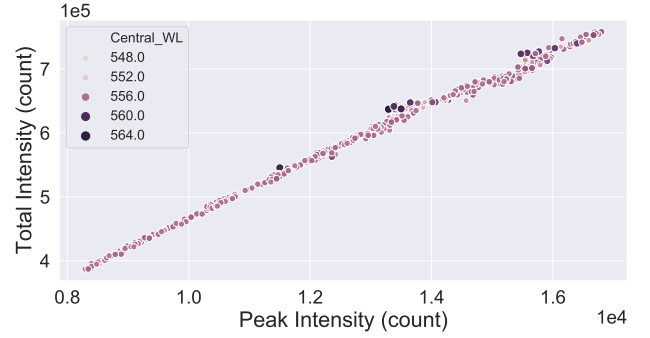


**Figure 10:** Peak intensity vs. total intensity of the LED source measured by the spectrometer. The linear scaling indicates that the shape of the LED spectrum is stable

the diode's responsivity curve in the operating range 300nm – 1300nm

For a given power spectrum, the real (and unbiased) power can be found by integrating the area below the power spectrum. The measured (and biased) power can be calculated as follows. The measured raw current is equal to the total area below the curve obtained by multiplying the power spectrum elementwise by the responsivity curve. The measured power is therefore equal to this current divided by the responsivity at the peak wavelength. The bias in the measured power of the LED source is found to be 2.6%. The bias level is, of course, dependent on the position and the shape of the source's spectrum. In general, the bias can be corrected by taking the raw current reading and do the unit conversion using the weighted responsivity by the spectral content of the light.



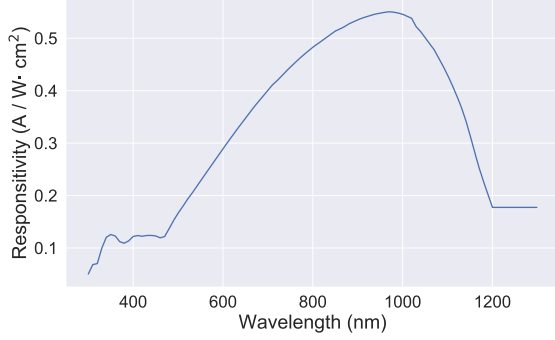


**Figure 11:** Photodiode responsivity curve over the operating wavelength 300nm – 1300nm. Before any measurement, the photodiode is initialised with responsivity at a single wavelength.

It should be noted that the calibration methods being developed are not only applicable to the current project but also useful for future experiments in OPMD. To name a few, the study of chromaticity dependence of the BFE requires knowledge of the spectral content of the source. The study of the point spread function (PSF) of spot illumination requires accurate measurements of flux. These studies are beyond the scope of this project but will be carried out in the OPMD in the future.

## 4 Flat-Field Illumination

The CCD is illuminated with the same LED source peaked at 556nm described previously. The operating temperature of the CCD is fixed at  $-95^{\circ}\text{C}$  throughout the experiments. Flat-field images are captured at two backside substrate voltage BSS = 0V and  $-60\text{V}$  and two collection gate widths  $w = 3\mu\text{m}$  (one gate open) and  $w = 5\mu\text{m}$  (two gates open) respectively. For each BSS and gate width, 400 pairs of flat-field images are taken from zero illumination up to the full well (by gradually increasing integration time from 0s to 5s).

The variance and correlations are calculated based on the difference between the frame pairs in order to eliminate fixed-pattern noise (e.g. variation in pixel size, quantum efficiency or spatial non-uniformity in illumination). This is done because spurious variance and correlations will be introduced if pixels have different responses to the same amount of light.  $R_{kl}$  represents the correlation between pixels separated by  $k$  columns and  $l$  rows apart. The covariance divided by the mean  $R_{kl} = C_{ij}/\mu$ , instead of by the variance  $C_{00}$ , is adopted as the equation for  $R_{kl}$  because the latter is itself affected by the brighter-fatter effect. The variance and correlations of the differenced frame are divided by a factor of two because the random noise component of the difference between two identical frames increases by the square root of two. [7]

According to the central limit theorem (CLT), the sta-

tistical precision of the variance and all correlation are  $1/\sqrt{N}$  where  $N$  is the number of pixels in each channel. The CCD E2V-250 has  $(4096 \times 4096)/16$  pixels per channel, giving a precision of 0.1%. <sup>4</sup>

### 4.1 Data Pre-Processing

The raw flat-field images need to be processed before any summary statistics can be obtained. First of all, any signal-independent signature (primarily the bias offset plus dark current) are subtracted from each channel of the CCD row by row using the overscan readout in the serial direction. The overscan is a section of the CCD that corresponds to clock and readout cycles beyond the physical pixels. [4] It is taken along with every image and records the offset and noise situation at the same time as the frame is taken. This is equivalent to taking bias frames and dark frames individually. Then, 20 pixels from all four sides of each channel are removed. These pixels are removed as the sensor response near the edges varies rapidly due to distortion to the drift field by guard ring voltages [3].

Finally, all bad pixels are masked, typically coming from cosmetic defects and spurious signals (e.g. cosmic rays), using the algorithm outlined in Guyonnet, A., et al. [6] A pixel is masked if it is  $3\sigma$  above a local average (over rectangles of  $128 \times 128$  pixels) and that there are more than two other pixels above  $3\sigma$  in their  $\pm 1$  pixel surrounding. These masks are applied to both the original image pairs and their difference. However, this masking strategy also removes some real variance inherent in Poisson statistics. A toy simulation shows that this on average leads to a loss of 1.35% of variance at all flux levels, while it will be shown later that the deviation of PTC from the expected photon variance is clearly not linear and can be as high as 25%.

### 4.2 PTC Analysis

The behaviour of variance and neighbour correlations changes abruptly once full well is reached, seen as a sudden fall in variance and a blooming effect in correlations. A margin of 10% below this saturation is chosen, up to which level the study of PTC and correlation maps is carried out. Figure 12 illustrates the raw PTCs plotted for four channels of CCD E2V-250 with BSS= $-60\text{V}$  and gate width  $=5\mu\text{m}$  in linear space. Channel 7 displays a very different response characteristic from the other channels, mainly due to lower amplifier gain configuration. The actual CCDs in the LSST telescope are carefully calibrated with consistent camera gain across all channels.

The raw PTCs can be scaled to the same magnitude using gain  $G$  expressed in (el/ADU). Traditionally,  $G$  is fitted using a straight line to the shot-noise dominated portion of the log-log PTC where the slope is

<sup>4</sup>Except that 20 pixels are trimmed off from each edge and additional pixels are excluded due to the masking strategy. Therefore, lower statistical power is more reasonable.

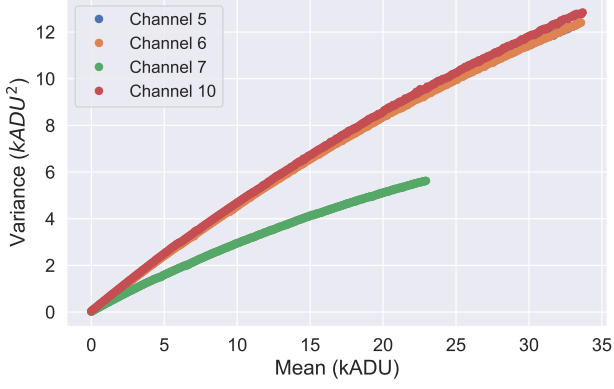


**Figure 12:** Raw PTCs plotted in arbitrary digital unit (ADU) from zero illumination upto 90% of the full well. Channel 7 has a different response behaviour compared to other channels.

1/2. The intercept of this line at  $\sigma_S[\text{ADU}] = 1$  gives the value of  $G$ . This method assumes pure photon noise in accordance with Equation 1. However, as suggested in [12], the raw PTC should be fitted with a second-order polynomial

$$\sigma_S^2 [\text{ADU}^2] = \frac{1}{G} S [\text{ADU}] + \beta S^2 [\text{ADU}^2] \quad (4)$$

where  $\beta$  is a dimensionless empirical coefficient to describe the non-linearity of the PTC. An interpretation for this quadratic correction and the physical significance of  $\beta$  will be presented in Section 5. To give a sense of the magnitude of the parameters, the fitted  $G = 2.036 \text{ el/ADU}$  and  $\beta = -3.710 \times 10^{-6}$  for channel 5, using the section up to the extremum. Depending on the range in the PTC being used, the discrepancy in  $G$  obtained from the two methods can be as high as 15%. The quadratic form describing the scaled curve is

$$\sigma_S^2 [\text{ADU}^2] \cdot G^2 = S [\text{ADU}] \cdot G + \beta S^2 [\text{ADU}^2] \cdot G^2$$

$$\sigma_S^2 [\text{el}^2] = S [\text{el}] + \beta S^2 [\text{el}^2] \quad (5)$$

parametrized by the same non-linearity coefficient  $\beta$ . Departures of the scaled PTCs (Figure 13) from photon variance  $\sigma_S^2 = \mu$  can be clearly observed. Besides, it is clear that deviations occur from the very beginning and have similar magnitude across all channels, indicating that the origin of this effect is to be found in the CCD instead of the downstream electronics. Near the full well, the variance deficit is nearly 25%. The residuals of linear and quadratic fit to the channel-averaged PTC are plotted at the bottom of Figure 13, justifying the form of second-order polynomial in Equation 5. A theoretical treatment of the quadratic correction will be presented in Section 5 with a electrostatic model. As a side remark, it should be noted that a small curvature occurs at the beginning of the residual of the quadratic fit. Fitting the PTC with higher-order polynomials does remove this pattern and gives a marginal improvement on the chi-square value. A consideration of the possible existence of higher-order correction terms is given in Appendix A.

Width \ BSS	0V	-60V
3 $\mu\text{m}$	$-4.110 \times 10^{-6}$	$-2.129 \times 10^{-6}$
5 $\mu\text{m}$	$-3.803 \times 10^{-6}$	$-1.823 \times 10^{-6}$

(a) Non-linearity coefficient  $\beta$

Width \ BSS	0V	-60V
3 $\mu\text{m}$	$2.283 \times 10^{-3}$	$2.162 \times 10^{-3}$
5 $\mu\text{m}$	$1.864 \times 10^{-3}$	$1.700 \times 10^{-3}$

(b) Correlation  $R_{10}$  measured at 60kel

**Table 1:** Non-linearity coefficient  $\beta$  and correlation  $R_{10}$  measured at BSS voltage = [0V, -60V] and gate width = [3 $\mu\text{m}$ , 5 $\mu\text{m}$ ]. The magnitude of  $\beta$  and  $R_{10}$  decrease as the BSS is turned on and the gate width widens, corresponding to increase in intensity and effective area of the drift field

### 4.3 Correlation

Spatial correlation between pixels is detected up to a distance of four pixels within the sensitivity limit of the CCD. From the correlation map at 60kel level in Figure 14, it is observed that correlation is the largest between the nearest neighbours and gradually decays as separation increases. It should be noted here that this observation is consistent with an electrostatic model, as the correlation due to electric field disturbances decays in free space as  $1/r^2$  and in a semiconductor as something more than  $1/r^2$  depending on screening. It is also clear that an anisotropy exists between amplitudes in the parallel direction and serial direction: the correlation  $R_{10}$  is about three times as large as  $R_{01}$ . However, this anisotropy tends to vanish at separations larger than 1 pixel. The pixel correlations are found to increase linearly with the mean fluxes among all spatial separations. The largest three correlations  $R_{10}$ ,  $R_{01}$  and  $R_{11}$  are shown in Figure 15.

The study of the brighter-fatter effect with different CCD settings should give us a clue about the origin of this effect. The non-linearity coefficient  $\beta$  and correlation  $R_{10}$  (measured at 60kel) are summarized in Table 1. It is clear that the coefficients depend on the backside substrate (BSS) voltage and the collection gate width, which separately controls the intensity and shape of the drift electric field. The linearity is shown to be gradually restored (manifested as a decrease in the magnitude of  $\beta$  and  $R_{10}$ ) as the drift field across the device is increased. This is an indication that the brighter-fatter effect is associated with some electromagnetic process. It cannot be explained by thermal diffusion alone, as suggested in some early works [9].

### 4.4 Restoring Linearity

The connection between PTC non-linearity and correlations can be illustrated by adding all covariances to the variance (Figure 16). On average, 97.2% of the variance is restored by aggregating the covariances



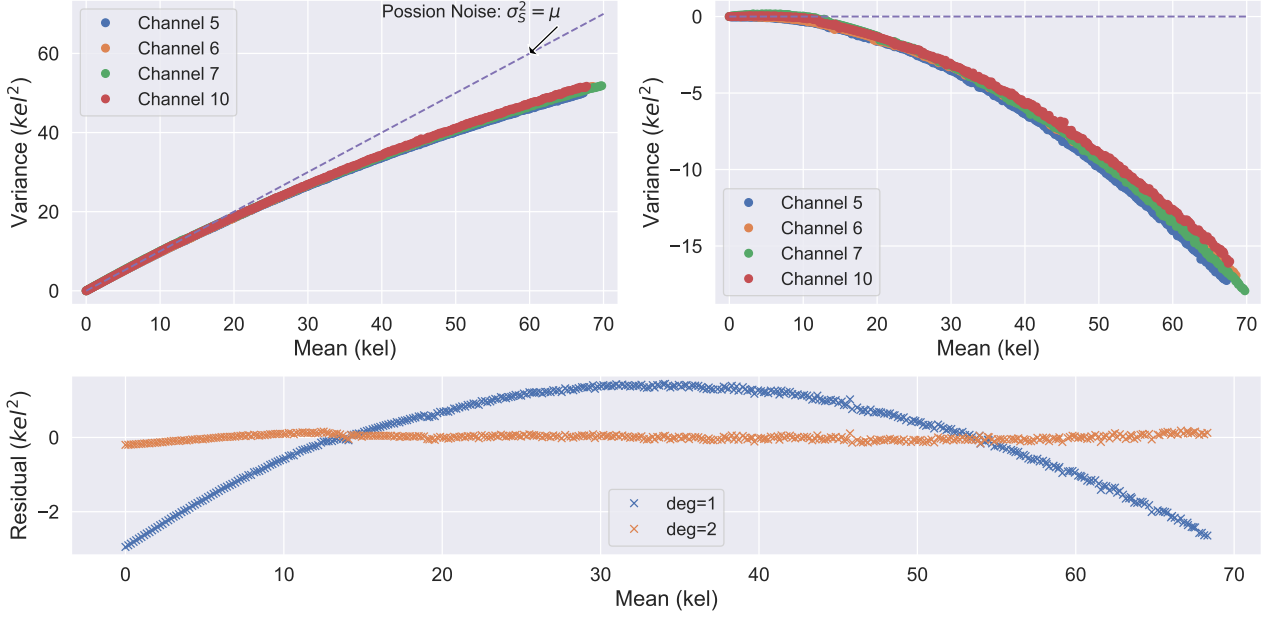


**Figure 13:** Top Left: Scaled PTC of four operating channels of CCD E2V-250 in the physical unit of electron charge. Departure from the expected Poisson photon variance  $\sigma_S^2 = \mu$  is observed. Top Right: Residuals of the scaled PTCs. They have identical magnitude and grow quadratically with the mean flux. Bottom: Residuals of linear and quadratic fit to the four-channel-average PTC

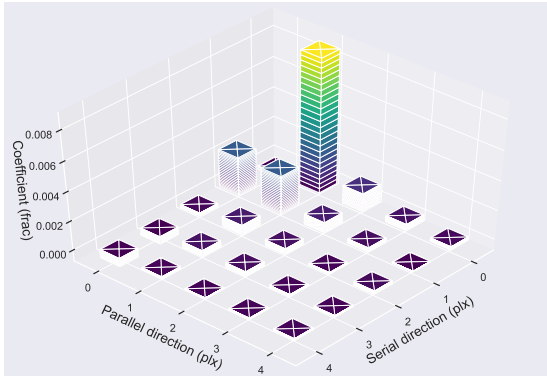


**Figure 14:** Flat-field correlation map at 60 keV along the parallel and serial direction. The correlation decreases as pixels get further apart. An anisotropy between the coefficients  $R_{01}$  and  $R_{10}$  is observed. The anisotropy tends to vanish for separation larger than 1 pixel.

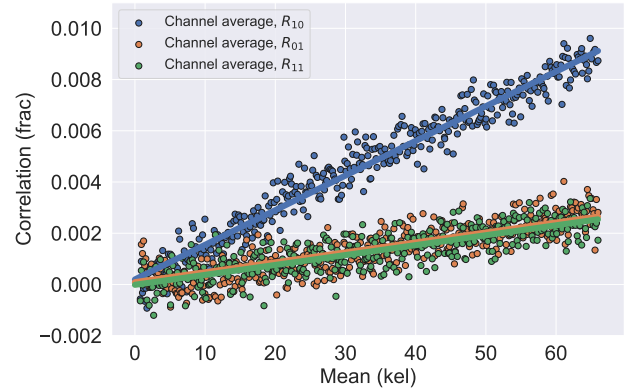


**Figure 15:** Correlations  $R_{10}$ ,  $R_{01}$  and  $R_{11}$  from the average of all four channels. The corrections are shown to increase linearly with the mean. The  $y$ -intercepts (not enforced to zero) are small for all channels.

## 5 Electrostatic Model

within the distance of 4 pixels. The remaining residual is attributed to correlations between pixels separated by more than 4 pixels and loss of Poisson variance during masking. As the correlations scale with the mean, the covariances are expected to scale with the square of the mean, which exactly compensates for the negative quadratic term in Equation 5. The recovery of linearity indicates that the brighter-fatter effect is linked to charge redistribution, which will be formally considered in Section 5. It is worth noting that linearity can be restored in a similar fashion for the raw PTCs, from which the channel gains can be fitted using linear regression after the corrections.

This section presents a physical model that provides the theoretical grounding for the brighter-fatter effect and accounts for the observed statistical properties of the PTC and correlation maps. The discussion largely follows along the lines of Antilogus et al. [1] with modifications. This model relies on the principles of electrostatics. It hypothesizes that charges collected in each pixel well, which increase during image integration, induce perturbations to the drift electric field in itself and its neighbours. Since same charge-carriers repel each other, the perturbation tends to drive newly arriving charges away from the pixel itself to nearby pixels, which can be considered equivalently as a de-

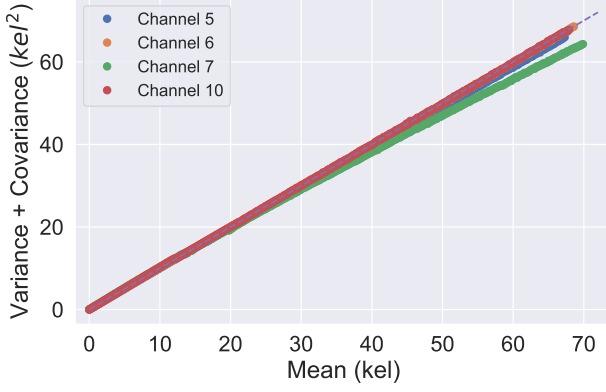


**Figure 16:** Corrected PTCs obtained by adding the sum of all covariances up to a distance of 4 pixels to the variance. On average, 97.2% of the variance or equivalently 88.8% of the deficit is restored compared to the expected mean = variance line.

crease in the effective size of the pixel. Overall, pixels with higher counts than their neighbours (due to Poisson fluctuation) repel more charges than they receive. Spatial correlations between neighbouring pixel values are established by this charge redistribution.

Figure 17 below extracted from Antilogus et al. [1] illustrates the phenomenon by superposing the drift electric field of empty pixels (black lines) and the Colombian perturbation caused by a pixel filled with  $50ke^-$  (red lines). The drift field is simulated with a depletion voltage (BSS) of 70V and a depth where charges accumulate of  $2.5\mu m$ . Pixels boundaries are found by following field lines from the top to the bottom of the pixels. The perturbation decreases the effective size of the pixel filled with electrons while increasing the size of its neighbours and shift their centroids slightly.

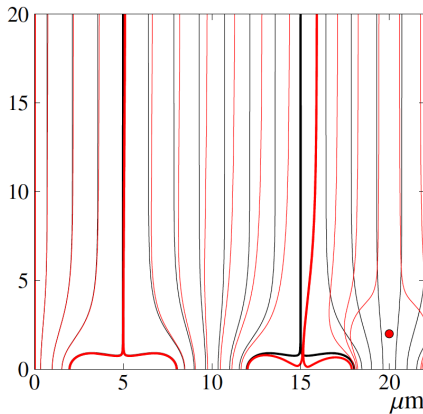


**Figure 17:** Drift electric field from depletion voltage (BSS) superimposed with Colombian electric field from collected charge inside CCD E2V-250 [1]

## 5.1 Electrostatic Model

In the electrostatic model, it is assumed that the perturbing electric field is directly proportional to the source charge (a prescription of electrostatics) and that the distortions to pixel boundaries are proportional to this perturbing field. Therefore, the displacement  $\delta_{00}^X$  of the effective boundaries of a pixel located at  $(0,0)$  that is far from the edges of the sensor in direction  $X$  can be expressed as

$$\delta_{00}^X = \frac{\alpha}{2} \sum_{ij} a_{ij}^X Q_{ij} \quad (6)$$

where  $\alpha$  is the real pixel size,  $a_{ij}^X$  are the time-independent ancillary pixel coefficients and  $Q_{ij}$  are charges stored in pixels at position  $(i,j)$  with respect to this “central” pixel. Thanks to parity symmetry, the  $a_{ij}^X$  coefficients only depend on the absolute value of  $i$  and  $j$ . The index  $X$  runs over the four possible 2D boundary directions. The factor of  $1/2$  accounts for the fact that on average, the perturbations to the drift electric field over the exposure time are half of what they are at the end of the exposure.<sup>5</sup>

The net signal charges transferred from the pixel  $(0,0)$  to a neighbour over the boundary  $X$  is given by

$$\Delta Q_{00}^X = \frac{\delta_{00}^X}{\alpha} \frac{(Q_{00} + Q_{00}^X)}{2} \quad (7)$$

where  $Q^X$  is the charge in the pixel to the neighbour of  $(0,0)$  in direction  $X$ . The assumption is that charge is stored uniformly throughout the entire pixel area, such that the amount of charge re-distribution is the charge density drifting on the boundary (average of the total charges in the pixels), weighted by the amount of boundary shift. The total charge in the pixel  $(0,0)$  after re-distribution is

$$\begin{aligned} Q'_{00} &= Q_{00} + \sum_X \Delta Q_{00}^X \\ &= Q_{00} + \frac{1}{4} \sum_X \sum_{ij} a_{ij}^X Q_{ij} (Q_{00} + Q_{00}^X) \end{aligned}$$

Next, the covariance of two observed pixel values is constructed

$$\text{cov}(Q'_{00}, Q'_{kl}) = \text{cov}(Q_{00} + \Delta Q_{00}, Q_{kl} + \Delta Q_{kl})$$

This expression can be expanded using the covariance’s distributive property,

$$\begin{aligned} \text{cov}(Q'_{00}, Q'_{kl}) &= \text{cov}(Q_{00}, Q_{kl}) + \text{cov}(Q_{00}, \Delta Q_{kl}) + \text{cov}(\Delta Q_{00}, Q_{kl}) \\ &= \begin{cases} \sigma_Q^2 + 2\text{cov}(\Delta Q_{00}, Q_{kl}) & \text{if } k, l = 0, 0 \\ 2\text{cov}(\Delta Q_{00}, Q_{kl}) & \text{if } k, l \neq 0, 0 \end{cases} \end{aligned}$$

where the second order term are dropped. The first term vanishes for  $k, l \neq 0, 0$  because the flat field illumination is spatially uncorrelated and is equal to  $\sigma_Q^2$

<sup>5</sup>This is, of course, an over-simplification of the charge build collection process. A more rigorous model is discussed in Appendix A.

if  $k, l = 0, 0$ , note that  $\sigma_Q^2$  is the variance of the “true” pixel values in the absence of perturbation (as opposed to measured). The second and the third term are equal from parity symmetry. Substitute the expression of  $\Delta Q_{00}$  and use again the distributive property of covariance

$$\begin{aligned} & \text{cov}(\Delta Q_{00}, Q_{kl}) \\ &= \frac{1}{4} \sum_X \sum_{ij} a_{ij}^X \text{cov}[Q_{ij}(Q_{00} + Q_{00}^X), Q_{kl}] \end{aligned}$$

On the assumption that the flat field illumination is spatially uncorrelated, the covariance between two pixel values satisfy  $\text{cov}(Q_{ij}, Q_{kl}) = \sigma_Q^2$  if  $(i, j) = (k, l)$  otherwise  $= 0$ . In the case where  $(k, l) \neq (0, 0)$  and  $(k, l)$  are not the nearest neighbour of  $(0, 0)$ ,  $Q_{kl}$  is uncorrelated with both  $Q_{00}$  and  $Q_{00}^X$ . Therefore, the covariance can be rearranged as

$$\begin{aligned} & \text{cov}(\Delta Q_{00}, Q_{kl}) \\ &= \frac{1}{4} \sum_X \sum_{ij} a_{ij}^X \text{cov}(Q_{ij}, Q_{kl}) \langle Q_{00} + Q_{00}^X \rangle \\ &= \frac{1}{4} \sum_X a_{kl}^X \sigma_Q^2 \langle Q_{00} + Q_{00}^X \rangle \\ &= \frac{1}{2} \sum_X a_{kl}^X \sigma_Q^2 \langle Q \rangle \end{aligned}$$

where the assumption of uniform pixel value expectation under flat field condition is used. This is the expression connecting the ancillary pixel values to the covariance in a flat field image. In the case where  $(k, l) \neq (0, 0)$  or  $(k, l)$  is the nearest neighbour of  $(0, 0)$ ,  $Q_{kl}$ , the expression is more complicated as the term  $(Q_{00} + Q_{00}^X)$  cannot be taken directly out of the covariance. This is explored in full by Antilogus [1]. After some additional algebra, the result ends up being the same as above.<sup>6</sup> Therefore, the full expression is

$$\text{cov}(Q'_{00}, Q'_{kl}) = \begin{cases} \sigma_Q^2 + \sum_X a_{kl}^X \sigma_Q^2 \langle Q \rangle & \text{if } k, l = 0, 0 \\ \sum_X a_{kl}^X \sigma_Q^2 \langle Q \rangle & \text{if } k, l \neq 0, 0 \end{cases}$$

The variance of pixel value  $Q'_{00}$  is a special case of  $\text{cov}(Q'_{00}, Q'_{00})$ . Using the property of Poisson distribution  $\sigma_Q^2 = \langle Q \rangle$ , the measured variance is found to be quadratic in the real signal mean  $\langle Q \rangle$

$$\text{var}(Q'_{00}) = \langle Q \rangle \left( 1 + \langle Q \rangle \sum_X a_{00}^X \right)$$

The correlation coefficients  $R_{kl}$  is found to scale with the illumination level of the uniform exposure, with the slope being the sum of all neighbouring ancillary pixel coefficients

$$R_{kl} = \frac{\text{cov}(Q'_{00}, Q'_{kl})}{\sigma_Q^2} = \sum_X a_{kl}^X \langle Q \rangle \quad \text{for } k, l \neq 0, 0$$

<sup>6</sup>The exact expression involves the third moment (or the skewness) of the charge probability density function proportional to  $\langle Q^3 \rangle - \langle Q^2 \rangle \langle Q \rangle$ . For a Poisson distribution, this term can be approximated to scale linearly with  $\sigma_Q^2 \langle Q \rangle$  and incorporated into the covariance. The relative error is of order  $1/\langle Q \rangle$ .

Note that  $a_{kl}^X$  are positive for  $k, l \neq 0, 0$  as charges stored in surrounding pixels tend to increase the pixel size of  $(0, 0)$ , whereas  $a_{00}^X$  is negative as the charge content in the pixel  $(0, 0)$  itself narrows its own boundary (see Figure 17).

### • Conservation of Covariance

This subsection shows that the PTC linearity is restored by adding the sum of covariances over all separations to the variance, consistent with the experimental observations

$$\begin{aligned} & \sum_{kl} \text{cov}(Q'_{00}, Q'_{kl}) \\ &= \text{var}(Q'_{00}) + \sum_{k, l \neq 0} \text{cov}(Q'_{00}, Q'_{kl}) \\ &= \langle Q \rangle \left( 1 + \langle Q \rangle \sum_X a_{00}^X \right) + \langle Q \rangle^2 \sum_X \sum_{k, l \neq 0} a_{kl}^X \\ &= \langle Q \rangle + \langle Q \rangle^2 \sum_X \sum_{kl} a_{kl}^X \end{aligned}$$

where the sum runs over positive, null, and negative  $kl$  pairs. If all charges  $Q_{kl}$  stored in the pixels are equal, the boundary does not shift at all. As a consequence, Equation (6) implies  $a_{ij}^X$  have to obey the sum rule  $\sum_X \sum_{kl} a_{kl}^X = 0$ . Therefore, the second term is always equal to zero and the sum

$$\sum_{kl} \text{cov}(Q'_{00}, Q'_{kl}) = \langle Q \rangle$$

which restores the linearity of the PTC anticipated by Poisson statistics.

## 6 Conclusion

In this investigation, the high power and wavelength stability of the throughput of the test system is verified, which is a requirement in most experiments carried out using the test system. Several useful calibration methods are developed, including spectral smoothing, deconvolution and bias removal. Next, the PTC non-linearity and linearly increasing spatial correlation between neighbouring pixels caused by BFE are illustrated. Linearity is restored by summing the variance and all covariances. The effects of BSS voltage and collection gate width on BFE is also discussed. Finally, electrostatic modelling of the charge collection process is studied to provide a theoretical basis of the observed statistical properties.

Lastly, it should be pointed out that the ultimate goal of studying BFE is to correct point-like real star images. Therefore, further work should be done to understand the BFE on compact point illumination. A more detailed charge collection model, for example, that takes into account the dynamic photon arrival process (e.g. as a Poisson process) should be considered. This investigation inevitably benefits any further work to be carried out in OPMD.

## References

- [1] Antilogus, P, et al. “The Brighter-Fatter Effect and Pixel Correlations in CCD Sensors.” *Journal of Instrumentation*, vol. 9, no. 03, 2014, doi:10.1088/1748-0221/9/03/c03048.
- [2] A. Savitzky and M. J. E. Golay, “Soothing and differentiation of data by simplified least squares procedures,” *Anal. Chem.*, vol. 36, pp. 1627–1639, 1964.
- [3] Astier, Pierre. “An Introduction to Some Imperfections of CCD Sensors.” *Journal of Instrumentation*, vol. 10, no. 05, 2015, doi:10.1088/1748-0221/10/05/c05013.
- [4] Astier, Pierre, et al. “The Shape of the Photon Transfer Curve of CCD Sensors.” *Astronomy and Astrophysics*, vol. 629, 2019, doi:10.1051/0004-6361/201935508.
- [5] Downing, Mark, et al. “CCD Riddle: a) Signal vs Time: Linear; b) Signal vs Variance: Non-Linear.” *High Energy, Optical, and Infrared Detectors for Astronomy II*, 2006, doi:10.1117/12.671457.
- [6] Guyonnet, A., et al. “Evidence for Self-Interaction of Charge Distribution in Charge-Coupled Devices.” *Astronomy and Astrophysics*, vol. 575, 2015, doi:10.1051/0004-6361/201424897.
- [7] Janesick, James R. *Scientific Charge-Coupled Devices*. SPIE Press, 2001.
- [8] Jiang, Lin-Qiao, et al. “SDSS J012119.10–001949.9: a Very Short Period M Dwarf Contact Binary from SDSS Stripe 82.” *Research in Astronomy and Astrophysics*, vol. 15, no. 12, 2015, pp. 2237–2243., doi:10.1088/1674-4527/15/12/011.
- [9] Ma, B., Shang, Z., Hu, Y., et al. 2014, in *Society of Photo-Optical Instrumentation Engineers (SPIE) Conference Series*, Vol. 9154, Society of Photo-Optical Instrumentation Engineers (SPIE) Conference Series, 1
- [10] Telescope, Large Synoptic Survey. “Vera C. Rubin Observatory Science Goals.” *Vera C. Rubin Observatory Science Goals — Legacy Survey of Space and Time*, www.lsst.org/science.
- [11] Weatherill, D.p., et al. “An Electro-Optical Test System for Optimising Operating Conditions of CCD Sensors for LSST.” *Journal of Instrumentation*, vol. 12, no. 12, 2017, doi:10.1088/1748-0221/12/12/c12019.
- [12] Weatherill, Daniel Philip. “Charge Collection in Silicon Imaging Sensors.” *Thesis (PhD) - Open University*, 2016.
- [13] Weatherill, Daniel. “OPMD LSST Sensor Testing / Foxtrot.” *GitLab*, gitlab.physics.ox.ac.uk/OPMD-lsst/foxtrot.

## A Dynamic Model

The static model gives a reasonable explanation for the non-linearity of the PTC. However, it over-simplifies the charge build-up process by imposing the assumption that the overall perturbations to the drift electric field are half of what they are at the end of the exposure. The model a) ignores the time dependence of the charge collection process b) expresses the pixel boundary shift in terms of the original unprimed charges (instead of the primed redistributed charges). In fact, as shown in Section 4, there is evidence that the second-order polynomial does not provide the best fit, suggesting that the most accurate parametrisation of PTC might require higher-order terms.

Relaxing the assumptions and take into account the time-dependent nature of the charge collection, we can express the shift  $\delta_{00}^X$  in pixel boundary as a function of the redistributed charges  $Q'_{ij}(t)$

$$\delta_{00}^X(t) = a \sum_{ij} a_{ij}^X Q'_{ij}(t)$$

The time derivative of the redistributed charges can thus be written as

$$\dot{Q}'_{00} = I \left[ 1 + \sum_{ij} a_{ij} Q'_{ij} \right]$$

where  $I = \dot{Q}_{00} = \dot{Q}_{00}^X$  is the current that would flow in each pixel in the absence of perturbations, for uniform flatfield illumination.<sup>7</sup> We have also combined the ancillary coefficients  $a_{ij}^X$  for each boundary into  $a_{ij} = \sum_X a_{ij}^X$  for the whole pixel area. Astier, Pierre, et al. showed that this leads to a time-derivative of the covariance between pixel (0,0) and (k,l) in the following form

$$\frac{d}{dt} \text{cov}(Q'_{00}, Q'_{kl}) = \delta_{0k} \delta_{0l} \langle Q \rangle + 2I \sum_{ij} a_{ij} \text{cov}(Q'_{kl}, Q'_{ij})$$

where  $\delta$  is the Kronecker delta that is non-zero only if  $(k, l) = (0, 0)$ . The same authors showed that the differential equation can be Fourier transformed and solved in the reciprocal space as a series of powers of  $t$ . The final solution in the pixel space reads

$$\text{cov}(Q'_{00}, Q'_{kl}) = \langle Q \rangle \left[ \delta_{0k} \delta_{0l} + a_{kl} \langle Q \rangle + \frac{2}{3} [\mathbf{a} \otimes \mathbf{a}]_{kl} \langle Q \rangle^2 + \frac{1}{3} [\mathbf{a} \otimes \mathbf{a} \otimes \mathbf{a}]_{kl} \langle Q \rangle^3 + \dots \right]$$

where the symbol  $\otimes$  refers to discrete convolution  $[\mathbf{a} \otimes \mathbf{a}]_{kl} = \sum_{ij} a_{ij} a_{k-i, l-j}$ . The  $n^{\text{th}}$  power of  $\langle Q \rangle$  decays as  $2^n / (n+1)!$ .

<sup>7</sup>In an even more detailed model, one could model the charge arrival as a Poisson process